Bio-Design and Manufacturing (2026) 9:63–79
https://doi.org/10.1631/bdm.2500456

RESEARCH ARTICLE

AI-driven interpretation and prediction of embedded printability based on rheology

Xianhao Zhou[1,3,4] · Zhenrui Zhang[1,3,4] · Jintian Yu[5] · Lixi Ma[1,3,4] · Sicheng Ma[1,3,4] · Bingyan Wu[1,3,4] · Zixuan Wang[1,3,4] · Ting Zhang[1,2,3,4] · Yongcong Fang[1,2,3,4] · Zhuo Xiong[1,2,3,4]

Received: 4 September 2025 / Accepted: 27 November 2025

Abstract

Embedded printing is a highly promising approach for creating complex structures within a yield-stress support bath. However, the accurate prediction and control of printability remain fundamental challenges due to the complex interactions between inks and support baths. Here, we present an artificial intelligence (AI)-driven framework that interprets and predicts embedded printability using rheological data. Using a standardized workflow, we extracted 21 rheological descriptors and established 12 indicators to evaluate structural continuity and geometric fidelity. Interpretable machine learning models revealed that direction-dependent defects are governed by the synergistic interplay among ink yield stress, support bath zero-shear viscosity, flow behavior index, and time constant. To enable the prediction of printability in a generalizable manner, we further developed a cascaded neural network, which achieved mean relative prediction errors below 15% across all indicators. Experimental validation using three-dimensional (3D)-printed constructs and micro-computed tomography (μCT) reconstructions confirmed a strong correlation between predicted and actual fidelity. This work establishes a physics-informed, data-driven paradigm for decoding and optimizing embedded printing, offering broad applicability and providing a robust tool for the rapid pairing of suitable printable ink–support bath combinations.

✉ Yongcong Fang
fangyc@tsinghua.edu.cn

✉ Zhuo Xiong
xiongzhuo@tsinghua.edu.cn

[1] Biomanufacturing Center, Department of Mechanical Engineering, Tsinghua University, Beijing 100084, China

[2] State Key Laboratory of Tribology in Advanced Equipment, Tsinghua University, Beijing 100084, China

[3] “Biomanufacturing and Engineering Living Systems” Innovation International Talents Base, Beijing 100084, China

[4] Biomanufacturing and Rapid Forming Technology Key Laboratory of Beijing, Beijing 100084, China

[5] School of Medicine, The Chinese University of Hong Kong, Shenzhen 518172, China

Graphical abstract

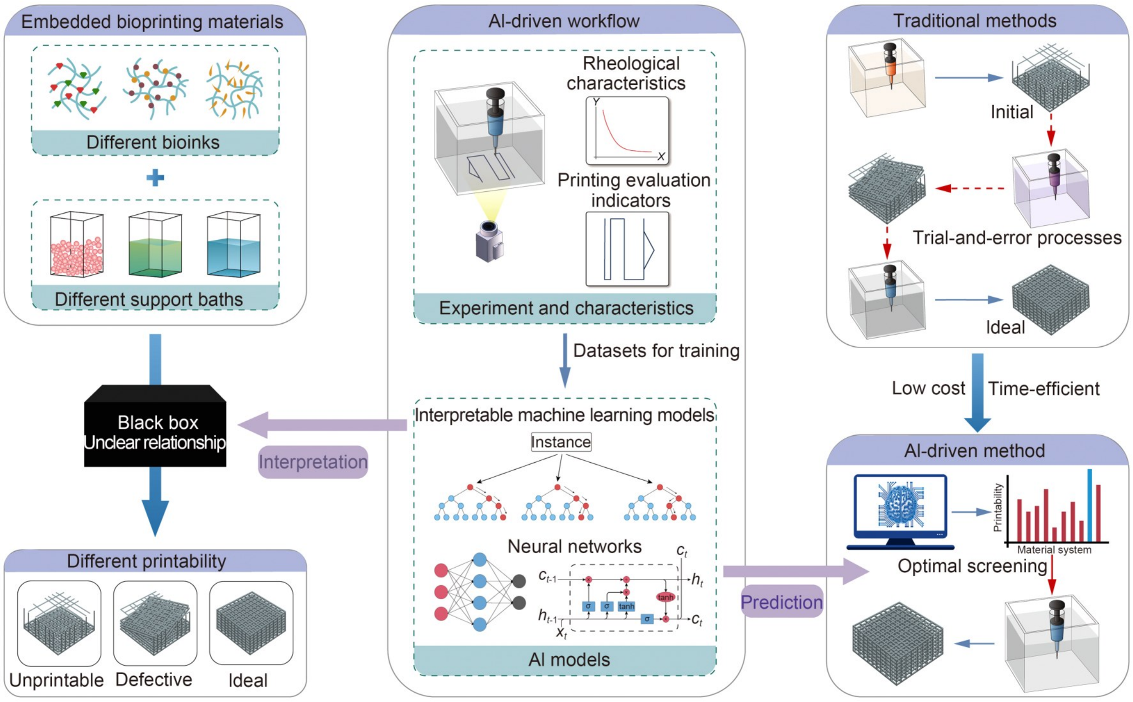

Keywords Embedded bioprinting · Printability · Rheology · Machine learning · Neural network

1 Introduction

The rapid evolution of manufacturing technologies has led to the emergence of embedded printing as a transformative approach for fabricating intricate soft-matter architectures [1–5]. By employing a yield-stress support bath to stably confine deposited inks, this technique enables the construction of complex geometries while accommodating the use of low-viscosity inks. These capabilities confer embedded printing with the potential to expand into diverse biomedical applications, including tissue engineering and regenerative medicine [6, 7]. Despite these advantages, the widespread adoption of embedded bioprinting is obstructed by various critical challenges, particularly the reliable enhancement of printability to ensure structural fidelity in complex three-dimensional (3D) constructs [8–13]. The vast diversity of bioink formulations and the intricate, often nonlinear interactions between bioinks and support baths significantly impede the rational design of compatible materials [14–16]. As a result, current efforts at optimization are largely empirical, relying on trial-and-error processes tailored to specific material pairs.

Previous studies primarily explored narrow subsets of material combinations, focusing on how variations in formulation ratios, concentrations, and printing parameters influence printability qualitatively [17–21]. However, such approaches suffer from inherent limitations. First, they are time-consuming, resource-intensive, and prone to batch variability and human subjectivity. Second, the resulting design principles can often not be transferred across materials, which limits their generalizability. Compounding these issues is the challenge of quantifying print fidelity, as an essential indicator of printability, in embedded contexts. Overhanging and free-form geometries resist standard morphological analysis, while poor optical transparency and thick exteriors obscure internal features. As such, advanced imaging techniques such as micro-computed tomography (μCT) and optical coherence tomography are often needed for accurate characterization, further exacerbating the complexity and cost [22]. Together, these challenges have significantly impeded the rapid, scalable advance of embedded bioprinting technologies.

Recently, the advent of artificial intelligence (AI) has introduced powerful computational tools that are reshaping the field of bioprinting [23–26]. In material design, AI-driven approaches have enabled the systematic modeling and prediction of hydrogel properties across diverse formulation spaces. These approaches capture a wide range of physicochemical and biological characteristics, including mechanical strength [27–30], degradation kinetics [31, 32], gelation dynamics [33, 34], swelling behavior [35–38], rheological parameters [39–41], and biocompatibility [42], accelerating and rationalizing material optimization. Efforts to enhance printability and structural fidelity have also benefited from AI integration. For example, Nadernezhad and Groll [43] investigated the effects of rheological modifiers on bioink behavior, providing interpretable guidelines rooted in physical principles. Meanwhile, Daly et al. [44, 45] employed real-time imaging and machine vision algorithms to identify printing defects and implemented closed-loop feedback control to dynamically adjust printing parameters when defects emerge, improving consistency and precision. These pioneering applications underscore the potential of AI to transform extrusion-based bioprinting, enabling both accelerated material development and process optimization.

Despite these advances, AI applications in embedded bioprinting remain underexplored. In particular, the central challenge of quantifying and predicting compatibility between bioink and support bath remains unresolved. Unlike extrusion printing, embedded bioprinting introduces an additional layer of complexity through the dynamic, nonlinear interactions between ink rheology and the mechanical properties of the support bath. These interactions critically influence print fidelity, but are poorly captured by current heuristic or material-specific frameworks. To bridge this gap, there is a pressing need for a generalizable, data-driven methodology that not only elucidates the physical significance of rheological features in governing embedded printing outcomes, thereby providing guidance for material design, but also predicts printability quantitatively, in order to boost the efficiency with which such systems can be designed.

In this work, we systematically investigated the role of rheology in determining printability within the field of embedded bioprinting and explored the potential of AI to speed up the design and screening of materials. In this work, rather than accounting for external factors such as printing parameters or environmental conditions, we focused specifically on intrinsic rheological features and their influence on printability [46]. To this end, we constructed a curated dataset comprising diverse combinations of bioinks and support baths, spanning a range of compositions and concentrations. For each pairing, we extracted 21 rheological descriptors alongside 12 printability metrics derived from specialized geometric test patterns. Using interpretable machine learning models, we elucidated how rheological parameters influence printability outcomes. These results were then contextualized in relation to the physical principles of embedded bioprinting, revealing generalizable rules and mechanistic insights that inform rational material design. To confer the ability to predict printability, we further developed a cascaded neural network integrating a long short-term memory (LSTM) network with a multilayer perceptron (MLP), allowing the direct, quantitative prediction of printability based on raw rheological data (replacing the characteristic parameters obtained by rheological formula fitting). Validation with unseen materials and 3D-printed constructs confirmed the model's predictive accuracy and practical utility, significantly reducing the reliance on exhaustive trial-and-error testing and expensive characterization methods. Notably, our findings revealed the potential for our framework to be generalized across materials, even those without shear-thinning rheological profiles, extending its applicability beyond conventional hydrogels (Fig. 1).

2 Results and discussion

2.1 Design of rheological features and indicators for evaluating the quality of printing

Embedded bioprinting has demonstrated the capacity to fabricate soft, complex structures using low-viscosity bioinks, even including those lacking shear-thinning properties. Nevertheless, shear-thinning remains a predominant rheological trait in both bioinks and support baths due to its critical role in enabling controllable deposition and structural stability. Specifically, for bioinks, shear-thinning facilitates continuous flow through the nozzle under high shear stress, while the viscosity of the bioinks is recovered upon deposition, ensuring shape retention. Moreover, in support baths, shear-thinning enables localized liquefaction in response to nozzle movement, allowing smooth translation of the nozzle and precise embedding of the extruded bioink [8, 9]. To ensure the generalizability of our findings, we constructed a comprehensive database of shear-thinning materials encompassing a wide range of types and concentrations (Table S1 in the supplementary information). The bioinks included inherently shear-thinning materials (e.g., gelatin methacryloyl) [47–50], as well as formulations modified to achieve tunable rheology (e.g., sodium alginate reinforced with nanoclay) [51–53]. Support baths were selected from two major categories: particle-based materials (e.g., gelatin microgels) [54, 55] and continuous-phase materials (e.g., carbopol) [56–60], which differ in the mechanisms underlying shear-thinning and viscoelastic response [10, 61].

To systematically characterize these materials, we focused on rheological descriptors—quantitative features that intrinsically define material behavior—rather than relying on nominal parameters like composition or concentration, which are less transferable across materials. Previous studies highlighted the importance of rheological behaviors such as shear-thinning, self-healing, and yield-stress in determining printability in embedded bioprinting [8]. Accordingly, we performed three core rheological tests—shear rate sweep, shear strain sweep, and alternating strain sweep—to obtain a comprehensive overview of the rheological profiles

(Fig. S1 in the supplementary information). From the curves obtained from these tests, we extracted 21 rheological features that collectively describe viscoelasticity, thixotropy, and phase transition behaviors: 10 features for bioinks and 11 for support baths (Fig. S2 and Table S2 in the supplementary information). To assess printability in a standardized and quantifiable manner, we designed planar test patterns based on the principle that any 3D path can be decomposed into orthogonal horizontal and vertical segments. This approach avoids occlusion and projection artifacts inherent in evaluating complex 3D constructs. The test pattern incorporated representative features such as straight lines, corners, and nodal junctions. A zigzag pattern with variable spacing was used to investigate fidelity at narrow and wide gaps, especially for right-angle geometries. In parallel with this, a triangular motif was introduced to evaluate obtuse-angle fidelity and nodal stability, which is common in branched architectures such as vascular networks.

To generate consistent data suitable for AI modeling, we established a standardized bioprinting and imaging workflow (Fig. S3 in the supplementary information). Printing was performed in predefined molds using fixed printing parameters, including nozzle diameter, speed, and extrusion rate. Each construct was imaged in situ using a custom-built imaging platform with fixed-focus macro cameras. Images were acquired from three orthogonal views—horizontal, vertical, and cross-sectional—with uniform focal length and resolution (Fig. 2a), enabling the acquisition of high-quality data for subsequent machine learning. We developed a comprehensive printability evaluation framework by extending prior work to include both qualitative and quantitative dimensions [12, 18] (Figs. 2b and 2c). Qualitative indicators captured global continuity (classified as "unprintable," "defective," or "ideal") and nodal continuity (classified as "connection" or "disconnection"). Quantitative indicators targeted local fidelity features affected by distinct modes of failure, including diffusion-induced deformation and overlapping deposition. Ten dimensionless metrics were defined, encompassing filament width and its variation, cross-sectional roundness and area, and angular fidelity at right and obtuse angles. These metrics collectively enabled a robust, fine-grained evaluation of fidelity loss and defect manifestation, forming the basis for subsequent model training and prediction. The specific methods for calculating these dimensionless parameters are summarized in Table 1.

2.2 Deciphering printability via an interpretable classification model

To systematically investigate the relationship between rheological properties and printability, we constructed a dataset encompassing 84 distinct materials. Each entry paired a rheological feature set with its corresponding printability evaluation outcomes, as previously described. We then

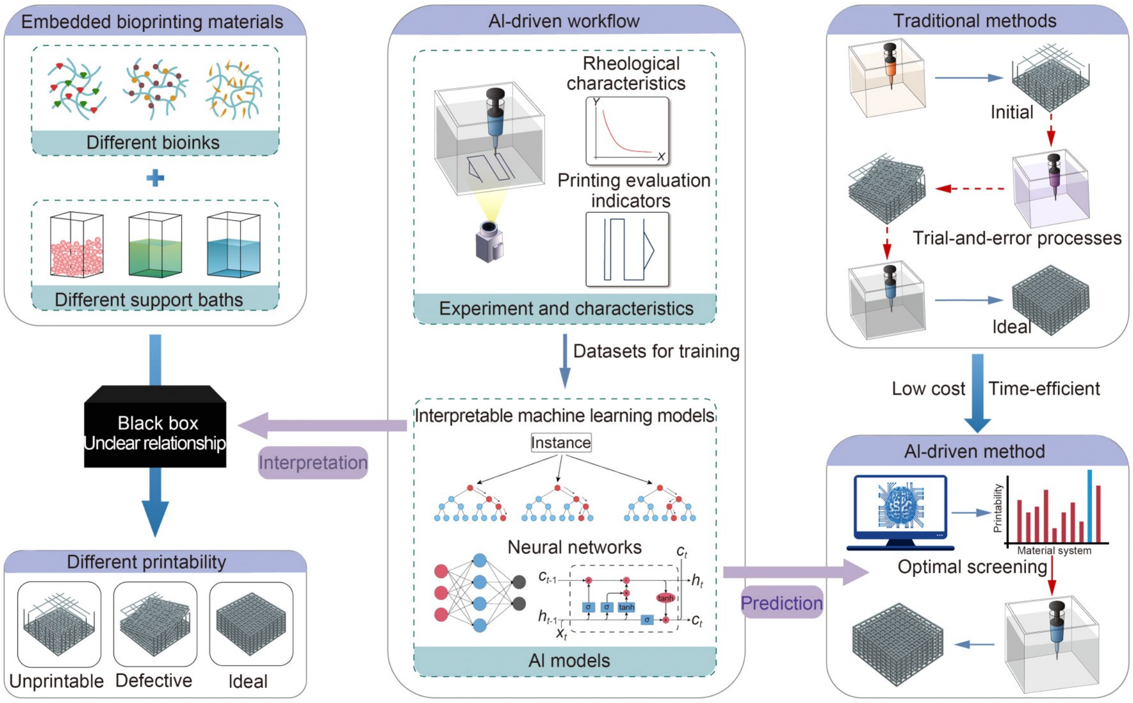

Fig. 1 AI-driven interpretation and prediction of printability in embedded bioprinting. Interpretable machine learning models were employed to elucidate the intrinsic relationship between rheological features and printability, offering mechanistic insights into the printing process and guiding rational material design. In parallel with this, a cascaded neural network was developed to directly predict printability from raw rheological curve data, enabling the efficient screening of compatible materials

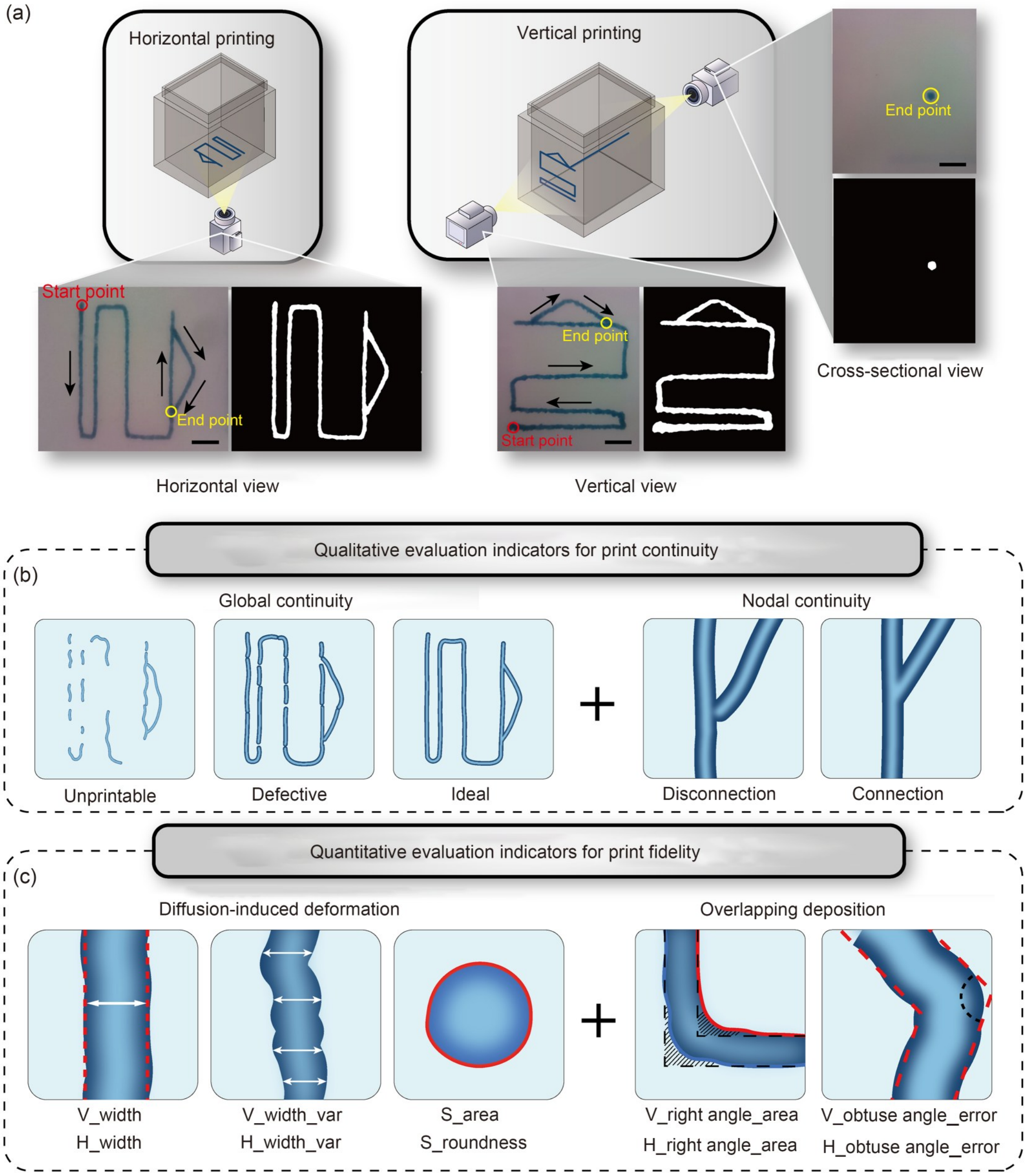

Fig. 2 Design and extraction of indicators for evaluating printability. (a) Acquisition of high-resolution multi-view images of printed constructs using fixed-focus macro cameras, followed by image preprocessing through binarization (146 pixels equal to approximately 1 mm, scale bars: 2 mm). (b) Two qualitative indicators used to assess print continuity. (c) Ten dimensionless quantitative indicators used to assess local print fidelity

applied interpretable machine learning models to uncover the rheological factors that fundamentally determine the performance of embedded bioprinting, with the aim of providing both mechanistic insights and practical guidelines for material formulation. We first trained a random forest (RF) classification model for predicting qualitative categories of printability (e.g., "ideal," "defective," "unprintable"), using 7-fold cross-validation to select optimal hyperparameters (N_estimators=125, Max_depth=25, Max_features=log2) based on the classification accuracy (Table S3 in the supplementary information). Feature importance analysis across 100 training iterations revealed that six rheological descriptors consistently contributed more than 25% above the average threshold (1/21≈0.0476), while the remaining features contributed less than 10% (Fig. 3a). These six dominant features were further categorized by their origin: (i) support bath-specific features: zero-shear viscosity and thixotropic time constant, and (ii) system-shared features: flow behavior indices and storage modulus at the yield transition point (for both components).

To interpret the influence of these features on print continuity, we employed partial dependence plots (PDPs). In

Table 1 Methods for calculating 10 dimensionless quantitative indicators reflecting local print fidelity

Local area	Quantitative evaluation indicator	Used parameter	Calculation method
Straight line	V_width	Actual average line width: W_{act}	$\frac{\mathrm{abs}(W_{\mathrm{act}} - W_{\mathrm{nom}})}{W_{\mathrm{nom}}}$
	H_width	Theoretical line width: W_{nom} (0.5 mm)	
	V_width_var	Variance of line width: $\mathrm{Var}_{\mathrm{w}}$	$\frac{\sqrt{\mathrm{Var}_{\mathrm{w}}}}{W_{\mathrm{act}}}$
	H_width_var	Actual average line width: W_{act}	
Cross section	S_area	Sectional area: A_{s}	$\frac{A_{\mathrm{s}}}{W_{\mathrm{act}}^2}$
		Actual average line width: W_{act}	
	S_roundness	Sectional area: A_{s}	$\frac{4 \times \pi \times A_{\mathrm{s}}}{C_{\mathrm{s}}^2}$
		Section perimeter: C_{s}	
Right-angle corner	V_right angle_area	Area of deviation zones: A_{r1}, A_{r2}	$\frac{A_{\mathrm{r1}} + A_{\mathrm{r2}}}{W_{\mathrm{act}}^2}$
	H_right angle_area	Actual average line width: W_{act}	
Obtuse-angle corner	V_obtuse angle_error	Actual obtuse angle: $\mathrm{Obt}_{\mathrm{act}}$	$\frac{\mathrm{abs}(\mathrm{Obt}_{\mathrm{act}} - \mathrm{Obt}_{\mathrm{nom}})}{\mathrm{Obt}_{\mathrm{nom}}}$
	H_obtuse angle_error	Theoretical obtuse angle: $\mathrm{Obt}_{\mathrm{nom}}$	

abs: function for calculating the absolute value

this analysis, we introduce the concept of a “continuity value” to characterize trends of print continuity. The continuity value is defined as the predicted score of continuity generated by the interpretable machine learning model, with a range from 0 (complete discontinuity) to 1 (ideal continuity). Values closer to 1 indicate stronger printability of the material system. One-dimensional (1D) PDPs revealed strong negative correlations between support bath-specific features and printability. As shown in Figs. 3b and 3c, higher zero-shear viscosity reduces the deformability and fluidity of the support bath, impairing its ability to locally yield and form a temporary cavity for the moving nozzle. Likewise, a longer time constant slows the recovery of the bath’s viscoelastic structure, undermining its capacity to re-solidify and support the printed construct. Among the system-shared features, the flow behavior index of the bioink exhibited a nonmonotonic relationship with continuity: Printability increased with the index to a critical point, and then declined (Fig. 3d). This suggests an optimal range of shear-thinning behavior: too little impedes flow, while excessive thinning compromises shape fidelity. Conversely, the support bath’s flow behavior index showed a monotonic negative correlation (Fig. 3e), indicating that stronger shear-thinning (lower index) consistently favors print continuity.

A two-dimensional (2D) PDP (Fig. 3f) highlighted the need for suitable features of both components in order to achieve optimal performance: High continuity was achieved when bioinks had a moderately high flow behavior index, while support baths had a markedly low one. This rheological synergy reflects the need for the support bath that liquefies more readily than the bioink under shear, enabling smooth nozzle traversal and precise extrusion while preventing excessive deformation or mixing at the interface. The modulus at the solid−liquid transition point (yield modulus) was also shown to be pivotal. For the bioink, a lower yield modulus favored uninterrupted flow (Fig. 3g), while for the support bath, a higher yield modulus enhanced its load-bearing capacity (Fig. 3h). The 2D PDP (Fig. 3i) demonstrated that optimal print continuity occurs when the support bath is approximately one order of magnitude stiffer than the bioink. This mismatch ensures that, under equivalent shear conditions, the bioink yields easily for deposition while the support bath maintains its structural integrity to confine and support the printed features. Together, these interpretable results provide quantitative confirmation of long-standing qualitative assumptions in the field of embedded bioprinting and provide a roadmap for the rational selection of appropriate bioink−support bath pairs. Specifically, these results highlight the need for differential shear-thinning and modulus asymmetry between components as rheological principles that play critical roles in determining printability.

2.3 Characterizing defect formation via an interpretable regression model

To shed more light on the quantitative factors underpinning print fidelity, we developed a regression-based model using a curated dataset of 50 materials that exhibited satisfactory print continuity. This step was necessary because quantitative shape descriptors cannot be obtained from fragmented or discontinuous prints. We trained an RF regression model for predicting quantitative fidelity metrics, using 5-fold cross-validation to select optimal hyperparameters (N_estimators=25, Max_depth=20, Max_features=5) based on the minimization of mean squared error (MSE) (Table S4 in the supplementary information). The relative prediction errors for the 10 dimensionless parameters in the validation set were all below 5%, further highlighting the model’s predictive accuracy.

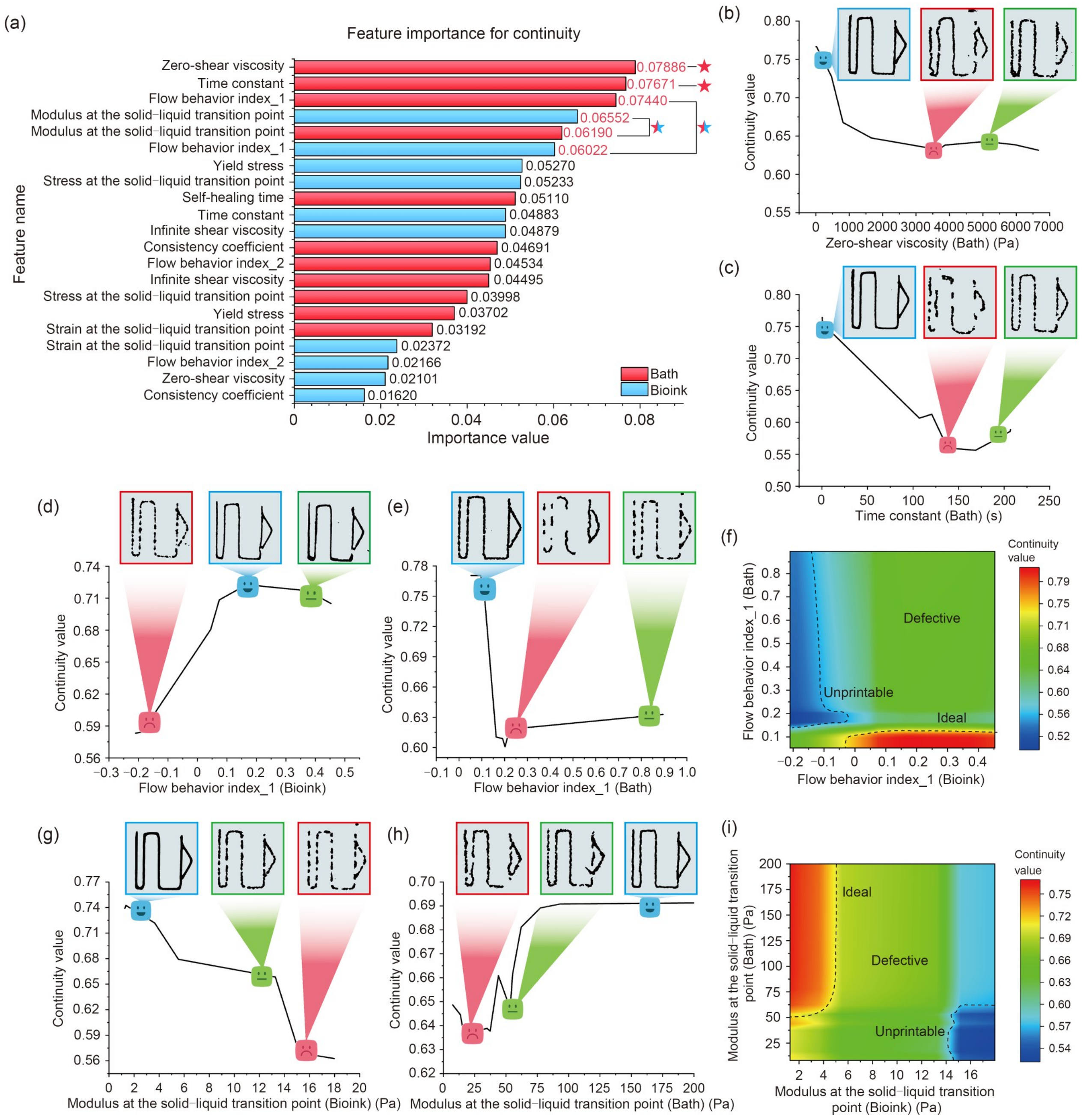

Fig. 3 Interpretable analysis of print continuity based on qualitative indicators. (a) Feature importance scores derived from an RF classification model. Rheological features with significant contributions to print continuity are indicated by asterisks, distinguishing those unique to the support bath from system-shared features. Influence of support-bath parameters: (b) zero-shear viscosity; (c) time constant. Effects and interactions of the flow behavior index: (d) bioink; (e) support bath; (f) combined effects of both components. Effects and interactions of the modulus at the solid–liquid transition point: (g) bioink yield modulus; (h) support-bath yield modulus; (i) combined effects of both components

Focusing on two representative types of printing defects—diffusion-induced deformation and overlapping deposition—we evaluated the directional and feature-specific contributions to defect formation. We averaged feature importance scores across 100 training iterations.

As shown in Figs. 4a and 4b, overlapping deposition defects were primarily governed by the rheological properties of the support bath, regardless of the direction of printing (horizontal or vertical). In particular, three parameters—thixotropic time constant, zero-shear viscosity, and yield stress—emerged as dominant predictors of such defects. Support baths with higher thixotropy exhibit more rapid structural rebuilding after shear, enabling effective filament confinement. Concurrently, elevated viscosity and yield stress promote rapid fluid-to-solid transition after nozzle traversal, minimizing uncontrolled filament spreading, especially

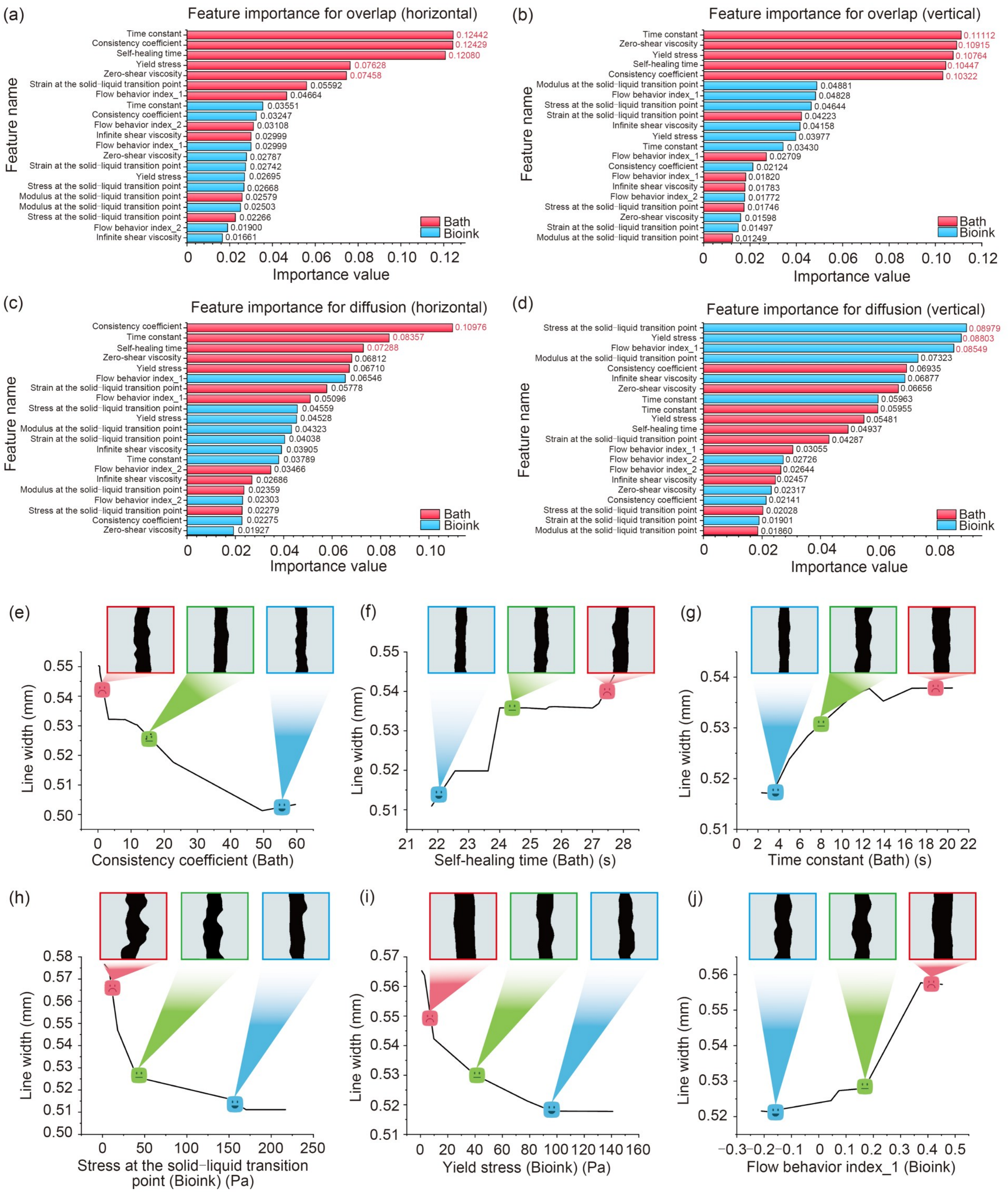

Fig. 4 Interpretable analysis of printing defects based on quantitative fidelity indicators. Feature importance scores for predicting defects arising from overlapping deposition under different printing directions: (a) horizontal; (b) vertical. Feature importance scores for predicting diffusion-induced defects under different printing directions: (c) horizontal; (d) vertical. Effects of support-bath rheological parameters on average line width under horizontal printing: (e) consistency coefficient; (f) self-healing time; (g) time constant. Effects of rheological parameters of bioink under vertical printing: (h, i) yield stress; (j) flow behavior index

upon changes in direction of the nozzle, such as at corners or junctions. In contrast, the rheological determinants of diffusion-related defects varied depending on the direction of printing. In the horizontal direction, support bath thixotropy remained the primary influence on printability (Fig. 4c), underscoring the importance of lateral resistance to bioink diffusion. However, in the vertical direction, bioink-specific features, particularly yield stress and flow behavior index, played more pronounced roles (Fig. 4d), suggesting a shift in the most important diffusion dynamics.

To obtain insights into the mechanisms behind these findings, we selected average printed line width as a quantitative proxy for fidelity and visualized the impact of key features using one-dimensional PDPs. For the support bath, we observed that reduced thixotropy—reflected by a lower consistency coefficient, longer time constant, and slower self-healing—resulted in significantly broader printed lines (Figs. 4e–4g). Similarly, for the bioink, lower yield stress and higher shear-thinning behavior led to increased spreading (Figs. 4h–4j). These observations align with directional diffusion mechanics: (i) Horizontally, diffusion occurs between the printed bioink filament and the surrounding support bath. Here, higher support bath thixotropy provides robust lateral confinement, suppressing horizontal spread. (ii) Vertically, diffusion is dominated by upward free diffusion into the transient cavity that forms behind the moving nozzle. In this regime, rapid gelation of the bioink—driven by higher yield stress and lower flowability—effectively limits filament deformation and maintains vertical fidelity. Taken together, these findings reveal direction-dependent interplay between bioink and support-bath rheology in determining defect formation. Notably, our interpretable regression framework not only achieved high predictive accuracy for metrics of print fidelity in shear-thinning materials but also provided clear physical insights that can guide future material development. These insights offer a principled basis for the rational design of materials suitable for high-fidelity embedded bioprinting, enabling the targeted tuning of thixotropy, yield-stress, and shear-thinning behavior to limit the formation of defects across spatial dimensions.

2.4 Extending generalizability and predictive capability via a cascaded LSTM-MLP neural network

Building on the mechanistic insights and predictive power of our previous models, we sought to enhance the framework's generalizability to include bioinks that do not exhibit shear-thinning. Conventional rheological fitting approaches have proven inadequate for these materials, as they failed to capture key nonlinearities in the relationships between shear stress and shear rate, and between viscosity and shear rate, thereby limiting the ability to extract informative features. To address this, we substituted fitted rheological parameters with raw rheological data, preserving the full temporal complexity inherent in these measurements. To maintain a comprehensive overview of the printing environment, we also retained critical descriptors of the support bath, specifically those related to the solid−liquid transition and self-healing time. We designed a novel cascaded LSTM-MLP neural network to effectively process and integrate these heterogeneous data modalities. In this architecture, the LSTM module acts as a sequence learner, extracting deep temporal features from the raw rheological curves treated as time-series data [62] (Fig. 5a). The extracted features are then concatenated with the conventional rheological features of the support bath and fed into the MLP module, which performs regression to predict a range of quantitative indicators of print fidelity (Fig. 5b).

For benchmarking, we established a baseline MLP model composed of two fully connected hidden layers and optimized its structure and hyperparameters via 5-fold cross-validation, arriving at an optimal configuration with 32 and 16 hidden nodes, respectively, and a dropout rate of 0.05 (Tables S5 and S6 in the supplementary information). To ensure a fair comparison, the MLP module within the cascaded neural network was constrained to a single hidden layer of 16 nodes, resulting in model complexity comparable to the baseline (Fig. 5c). Evaluation on the validation dataset (Figs. 5d and 5e) demonstrated that the cascaded neural network consistently outperformed the baseline MLP across nearly all quantitative indicators, achieving an average of more 50% reduction in MSE. Relative error metrics also showed systematic improvement. The greatest gains were observed for indicators where the baseline model struggled, highlighting the superiority of the cascaded neural network in terms of capturing complex relationships between rheological factors and printability.

To rigorously test the generalizability of this approach, we introduced two novel materials absent from the original dataset, namely, a bioink formulation of 5% gelatin methacrylate (GelMA) combined with 1% hyaluronic acid methacrylate (HAMA) [63, 64] and a support bath consisting of 9.6% gelatin microparticles [22, 65]. We constructed three experimental scenarios involving these new materials: (i) a known bioink paired with a novel support bath, (ii) a new bioink paired with a known support bath (1.5% xanthan gum (XG)), and (iii) both new bioink and support bath combined (Fig. S5 in the supplementary information). The cascaded neural network maintained relative prediction errors within ±15% across these diverse conditions (Figs. 5f−5h), highlighting its robustness and adaptability. Collectively, these findings demonstrate the ability of the cascaded neural network to extend the capacity to predict printability beyond classical shear-thinning bioinks, providing a scalable, accurate, and generalizable computational tool for evaluating and optimizing embedded bioprinting materials across a broad range of compositions and rheologies. This approach lays a solid foundation for the data-driven, high-throughput screening of materials and the selection of suitable bioink–support bath pairs in future biofabrication projects.

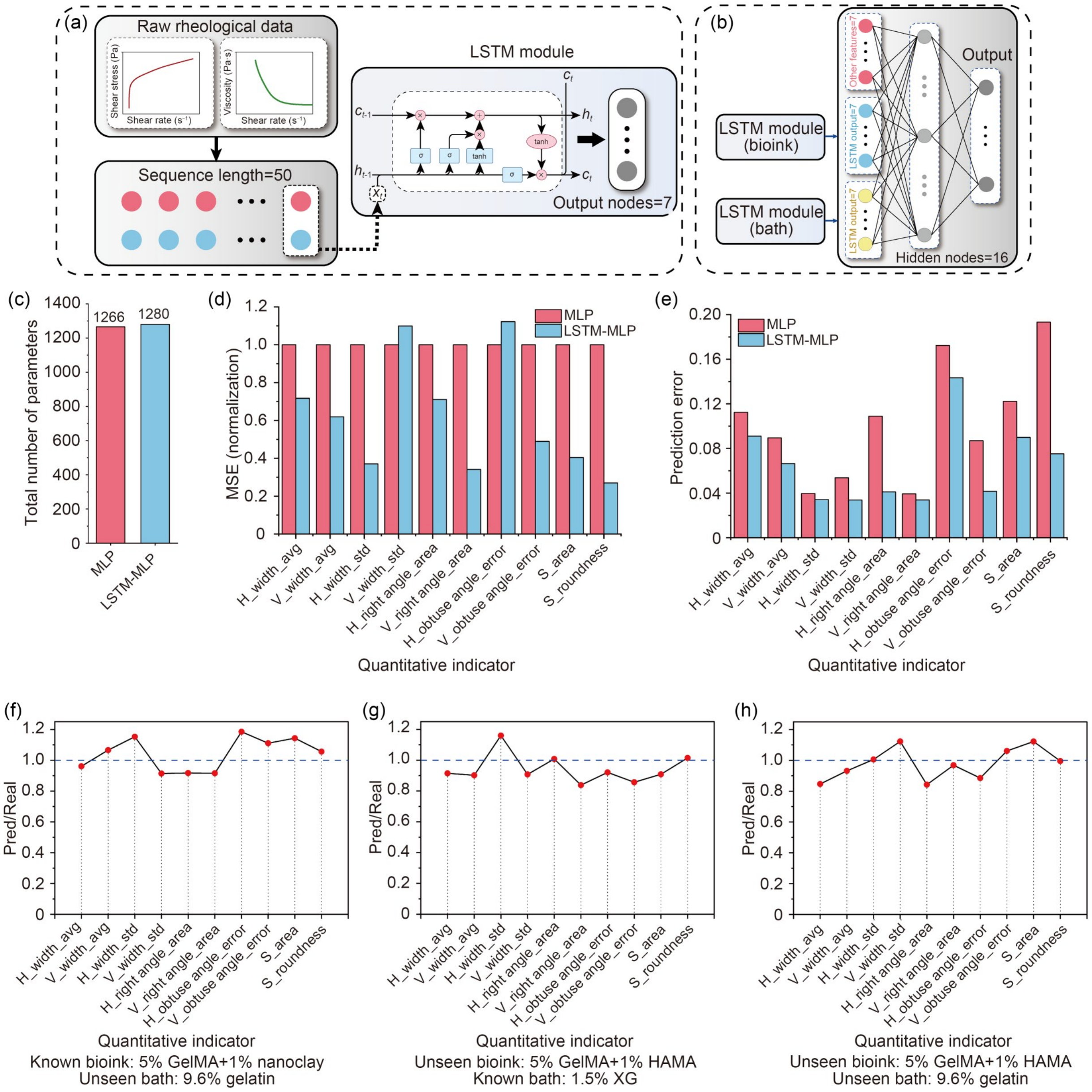

Known bioink: 5% GelMA+1% nanoclay
Unseen bath: 9.6% gelatin

Unseen bioink: 5% GelMA+1% HAMA
Known bath: 1.5% XG

Unseen bioink: 5% GelMA+1% HAMA
Unseen bath: 9.6% gelatin

Fig. 5 Quantitative prediction of printability using a cascaded LSTM-MLP neural network. Network architecture: (a) the LSTM module extracts temporal features from rheological curves; (b) the MLP module integrates these features to predict print fidelity. Comparison of model performance between the cascaded neural network and the baseline MLP model: (c) model complexity (parameter count); (d) MSE loss; (e) relative prediction error. Evaluation of model generalizability on unknown materials: (f) known bioink with unseen support bath; (g) unseen bioink with known support bath; (h) unseen bioink with unseen support bath

2.5 Validation of predictive performance through 3D bioprinting of complex structures

While the previous experiments mentioned above established the predictive accuracy of the cascaded neural network in standard 2D patterns, we sought to confirm its applicability to complex, multi-dimensional geometries, better reflecting real-world challenges in the field of biofabrication. Our long-term goal is to replace conventional, time-intensive, and resource-intensive iterative workflows with data-driven predictions, thereby speeding up the screening of materials and process refinement in embedded bioprinting. To this end, we selected three biomimetic 3D structures of increasing geometric complexity as test cases: (i) a tracheal construct characterized by concentric cylindrical rings, (ii) a liver model with gently undulating surfaces, and (iii) a cardiac model featuring intricate external contours and pronounced curvature. To facilitate neural network-based prediction, we calculated a normalized composite printability score by averaging the 10 quantitative evaluation indicators, comprehensively reflecting the impact of various defects on print fidelity. For printed constructs, high-resolution 3D reconstruction was performed using μCT, followed by rigid registration to the digital design models. Boolean operations were applied to identify mismatched volumes, and the fidelity of each print was assessed using the volume error ratio, defined as $V_{\mathrm{error}}/V_{\mathrm{real}}$, where V_{real} denotes the volume of the theoretical model (Fig. 6a). A lower value of this ratio indicates better print fidelity.

Using a fixed bioink formulation (5% GelMA + 1% nanoclay), we systematically varied the support-bath composition and printed all three 3D geometries (Fig. S6 in the supplementary information). Across all structures, a consistent order in terms of the fidelity emerged: the 2.0% alkali-swellable emulsion copolymer (AVC) support bath yielded the highest-fidelity prints, while the 0.5% AVC condition was associated with the most severe deviations. Intermediate performance was observed for 1.5% and 2.0% XG support baths, with 1.5% XG slightly outperforming the 2.0% one. Crucially, these empirical trends matched the neural network predictions based on the composite printability scores (Fig. 6b). Further qualitative support was provided by μCT reconstructions of the liver model under three representative conditions (0.5% AVC, 2.0% XG, and 2.0% AVC). As shown in Fig. 6c, the 2.0% AVC condition produced constructs that most accurately preserved the target dimensions and morphological features, achieving over 50% greater fidelity than the poorly performing 0.5% AVC support.

To test the consistency of predictions across different bioink formulations, we fixed the support bath at 1.5% XG and evaluated three different bioinks. Again, the neural network's predictions aligned well with actual print outcomes, supporting the ability of the model to generalize across various bioinks (Fig. 6d). Taken together, these findings demonstrate that the cascaded neural network can reliably predict 3D print fidelity across structurally diverse models and materials. This predictive power could be extremely valuable in eliminating the need for exhaustive experimental screening, enabling more rapid prototyping and optimization in embedded bioprinting. The model's robustness in complex geometries also supports its value in translational biofabrication workflows, where the selection of an appropriate combination of bioink and support bath is essential for achieving construct fidelity that is sufficient for clinical applications.

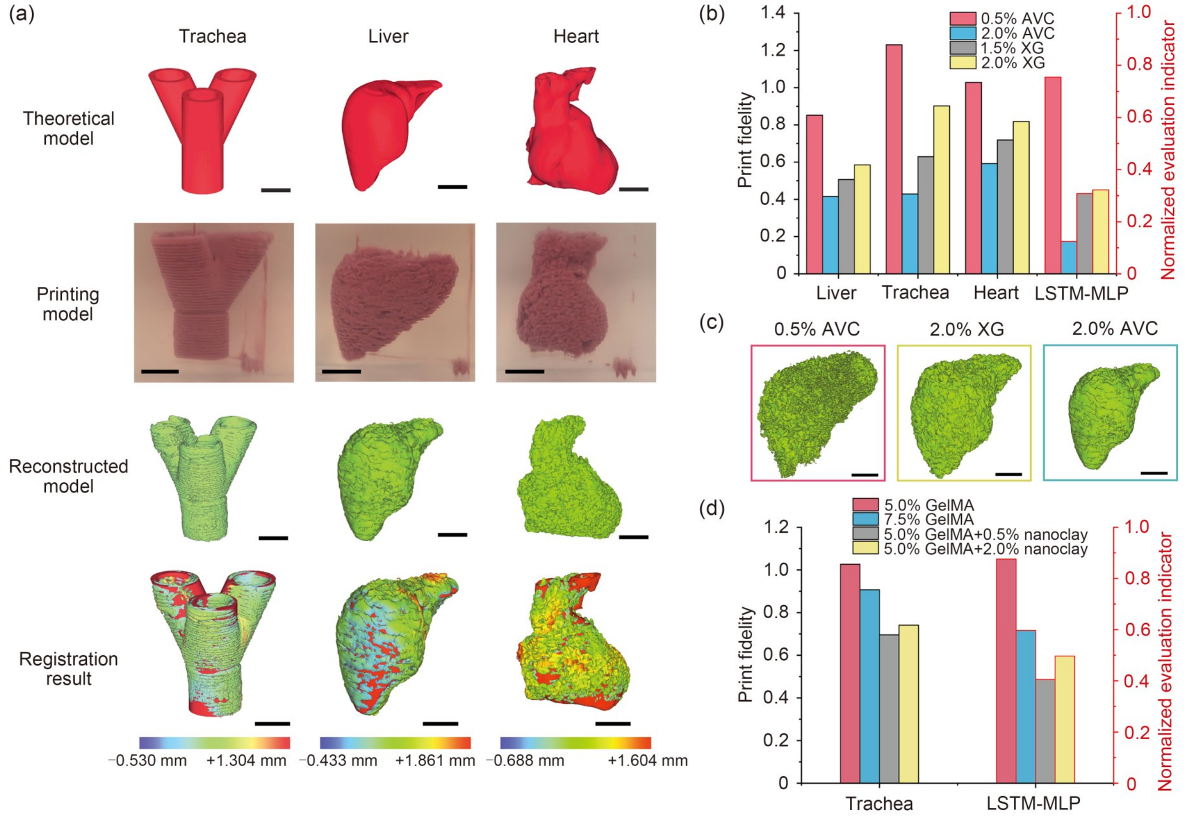

Fig. 6 Experimental validation of the cascaded neural network via 3D bioprinting. (a) Representative results of actual printing and corresponding 3D reconstructions, aligned with theoretical models (scale bars: 5 mm). (b) Comparison between predicted and experimentally measured fidelity across different support baths. (c) Representative 3D reconstructions of structures printed with different support baths (scale bars: 5 mm). (d) Comparison between predicted and experimental fidelity across different bioinks

3 Conclusions

For the precise and reliable fabrication of complex 3D constructs via embedded bioprinting, there is a need to enhance printability. However, conventional approaches for achieving this—rooted in empirical knowledge and iterative experimentation—are often inefficient, labor-intensive, and poorly generalizable across diverse materials. To overcome these limitations, we proposed an AI-driven framework that integrates mechanistic understanding and predictive modeling to accelerate the design and screening of combinations of bioink and support bath, as a way of promoting progress in the embedded bioprinting field. In terms of incorporating information on the mechanisms associated with printability, we employed interpretable machine learning models to elucidate how specific rheological features contribute to characteristic printing defects. This approach not only provided actionable insights into the physical origins of poor printability but also offered guidelines for the rational design of printable materials. In terms of creating a valuable predictive tool, we developed a cascaded LSTM-MLP neural network that combines raw rheological curves with features of support baths to deliver accurate, quantitative predictions of print fidelity. This model demonstrated robust performance across both known and previously unseen materials, significantly reducing the need for laborious and time-consuming experimental validation.

Despite these advances, various challenges remain. First, while the use of raw rheological curves allows broader applicability of this approach—including materials that do not undergo shear-thinning—the limited availability of such datasets currently restricts the possibility of performing comprehensive model training and validation. Second, our current feature set emphasizes universal rheological descriptors, which support generalizability but fail to include other important factors such as electrostatic interactions, surface tension, and swelling dynamics, each of which may affect printability under specific conditions. In addition, the influence of cell loading parameters—including cell volume fraction, size distribution, and morphology—on the rheological behavior of bioinks and subsequent printability has not yet been incorporated into our framework. Since cells can measurably alter viscosity, yield stress, and thixotropy, future efforts should systematically integrate cell-related descriptors into the dataset. Incorporating these biological factors alongside rheological, physicochemical, and interfacial properties will further enhance the generalizability of predictive models, ensuring their applicability to both acellular and cell-laden printing scenarios.

Looking forward, future work should first focus on expanding the training dataset to include a broader spectrum of bioinks and support baths, while also incorporating data on a range of different variables (e.g., physicochemical, biological, and interfacial properties). This would increase the diversity and representativeness of the data, which should in turn boost the robustness of predictive modeling. In parallel with this, it is important to introduce physical constraints and domain-related information into the modeling framework in order to improve reliability and interpretability. Approaches such as physics-informed neural networks or other hybrid architectures could help us to integrate governing physical principles with data-driven learning, resulting in models that are both more accurate and physically meaningful. The combination of enriched datasets and physics-informed AI architectures—including multimodal and transformer-based models—has the potential to deepen our understanding of the physics involved in such systems and enable us to generate more nuanced predictions of printability. Taken together, these advances should lay the groundwork for automated, intelligent, and precision-guided material design, ultimately accelerating the clinical translation of embedded bioprinting technologies for regenerative medicine, organ modeling, and tissue engineering.

4 Materials and methods

4.1 Bioink preparation

Materials: GelMA (degree of substitution: 60%; CAS: 9000-70-8), lithium phenyl-2,4,6-trimethylbenzoylphosphinate (LAP), HAMA (molecular weight (M_w)≈400 kDa; CAS: 9067-32-7), nanoclay, and blue nondiffusion hydrogel dye were purchased from EFL Inc., China. Sodium alginate (CAS: 9005-38-3) was obtained from Sigma-Aldrich, St. Louis, USA.

GelMA bioinks: GelMA was dissolved at 5.0% (50 g/L) and 7.5% (75 g/L) in a 0.025% (0.25 g/L) LAP solution prepared with dyed deionized (DI) water. The solution was stirred at 800 r/min and 37 °C for 1 h to ensure complete dissolution. To improve the rheological properties, nanoclay was added to the 5.0% GelMA solution at concentrations of 0.5% (5 g/L), 1.0% (10 g/L), and 2.0% (20 g/L), followed by stirring at 800 r/min for 1 h to achieve homogeneous dispersion.

Alginate bioinks: Sodium alginate was dissolved at 1.0% (10 g/L) and 2.0% (20 g/L) in dyed DI water and stirred at 1200 r/min for 3 h at room temperature until completely solubilized. Nanoclay was then incorporated at 1.0% (10 g/L) and 2.0% (20 g/L) and mixed for an additional 1 h at 1200 r/min.

GelMA–HAMA hybrid bioinks: HAMA was first dissolved at 1.0% (10 g/L) in dyed DI water with stirring at 1200 r/min for 4 h at room temperature. Subsequently, GelMA was added at 5.0% (50 g/L), and the mixture was stirred at 800 r/min and 37 °C for 1 h to achieve complete homogeneity.

Dye preparation: To facilitate the visualization of printed constructs, all DI water used in bioink formulations was premixed with 10% (100 g/L) blue dye and stirred for 1 h to ensure a uniform distribution.

4.2 Support bath preparation

Materials: AVC was obtained from Clariant, Switzerland. Carbomer (CAS: 9007-20-9) and sodium hydroxide (CAS: 1310-73-2) were purchased from Macklin, China. XG (CAS: 11138-66-2) was sourced from MedChemExpress (Monmouth Junction, USA), and agarose (CAS: 9012-36-6) from Amresco (Solon, USA). Type A gelatin (CAS: 9000-70-8), Pluronic F127 (CAS: 9003-11-6), and gum arabic (CAS: 9000-01-5) were all purchased from Sigma-Aldrich.

AVC-based baths: AVC powder was dissolved in DI water at 0.5% (5 g/L), 1.0% (10 g/L), and 2.0% (20 g/L) and stirred at 1200 r/min overnight at room temperature. Before use, the solution was centrifuged at 1200*g* for 5 min to eliminate air bubbles. The bath was stored at 4 °C for long-term use.

Carbomer-based baths: Carbomer was dispersed in DI water at 0.25% (2.5 g/L), 0.5% (5 g/L), and 1.0% (10 g/L) with vigorous shaking. The pH was adjusted to 7.0 using a solution of 2 mol/L sodium hydroxide under continuous stirring. The final solution was stored at 4 °C and centrifuged at 1200*g* for 5 min before use to eliminate air bubbles.

XG-based baths: XG was dissolved at 1.0% (10 g/L), 1.5% (15 g/L), and 2.0% (20 g/L) in DI water and stirred at 1200 r/min overnight at room temperature. The solution was stored at 4 °C and centrifuged at 1200*g* for 5 min prior to eliminating air bubbles.

Agarose-based baths: Agarose was dissolved at 0.5% (5 g/L), 0.75% (7.5 g/L), and 1.0% (10 g/L) in DI water by heating the mixture to 100 °C for 8 min. The solution was then cooled to room temperature under stirring at 600 r/min for 2.5 h to facilitate granular gel particle formation. The solution was stored at 4 °C and centrifuged at 500*g* for 3 min to eliminate air bubbles.

Gelatin microgel-based baths: Gelatin microgel support baths were prepared via a coacervation method, as previously reported [22]. Briefly, 6.4% (mass fraction) type A gelatin, 0.5% (mass fraction) Pluronic F127, and 0.2% (mass fraction) gum arabic were dissolved in boiling DI water. Upon complete dissolution, an equal volume of ethanol was added, and the beaker was sealed with parafilm to prevent evaporation. The solution was cooled to room temperature while stirring at 500 r/min overnight. The microgel was then collected via centrifugation at 500*g* for 3 min, washed three times with DI water to remove residual ethanol and pluronic, and stored at 4 °C. Before use, it was centrifuged at 1200*g* for 5 min to eliminate air bubbles.

4.3 Rheological characterization

Rheological measurements were conducted on all prepared bioinks and support baths using a rotational rheometer (MCR301, Anton Paar, Austria) equipped with a 25-mm parallel plate geometry. All experiments were performed at 20 °C under controlled environmental conditions, with three independent replicates for each material condition to ensure reproducibility.

Shear rate sweep: To assess shear-thinning behavior, shear rate sweep tests were performed by increasing the shear rate logarithmically from 0.01 to 1000 s^{-1}. A total of 250 data points were recorded for variables including shear rate, shear stress, and apparent viscosity. These data were used to generate viscosity−shear rate and shear stress−shear rate curves. To quantitatively describe the shear-thinning and thixotropic characteristics, the data were fitted using both the Carreau and Herschel−Bulkley models, with custom scripts implemented in MATLAB.

Shear strain sweep: To evaluate phase transition behavior, oscillatory strain sweep tests were conducted by increasing the shear strain from 1% to 2000%. A total of 200 data points for variables including shear strain, shear stress, storage modulus (G'), and loss modulus (G''), were collected on a logarithmic scale. The modulus–strain curve was analyzed to determine the yield point (i.e., the solid–liquid transition point), defined as the strain where $G' \approx G''$. Local linear fitting was applied to accurately identify this transition, and the corresponding shear strain, shear stress, and modulus values were extracted as rheological features indicative of gelation behavior.

Alternate strain sweep: To investigate the self-healing ability of support baths, alternate strain sweep tests were conducted by cyclically applying low (1%) and high (100%) shear strains. Each strain level was maintained for 25 s, and the cycle was repeated three times. Storage and loss moduli were recorded at 0.5-s intervals, resulting in a total of 300 data points. The modulus–time curve was plotted to visualize recovery behavior. The time required for G' and G'' to return to a steady state after each strain transition was measured, and the average of five recovery intervals was extracted as a rheological indicator of self-healing performance.

4.4 Printing experiments and printability analysis

All printing experiments were performed using a commercial bioprinter from TissHUe Biomedical Technology Co., Ltd., China. To ensure robustness, each printing experiment was performed in triplicate under identical conditions. A custom-fabricated printing container (15 mm×20 mm× 22 mm) and a matching positioning fixture were employed to maintain a fixed spatial alignment between the container and the printer nozzle. This setup ensured consistent initialization of the printed pattern based on a unified absolute coordinate system. Printing parameters were standardized across all experiments to ensure consistency and comparability. The speed of nozzle movement was set at 3 mm/s, and the material extrusion speed was maintained at 0.5891 mm³/s. A nozzle with an internal diameter of 0.51 mm (21G) was used, resulting in a theoretical filament width of approximately 0.5 mm, closely matching the nozzle diameter and enabling direct assessment of fidelity.

Following printing, the entire container—preserving the spatial integrity of the printed structure—was transferred to a custom-designed imaging station. This station was equipped with two fixed-focus macro cameras, enabling simultaneous acquisition of high-resolution RGB images from both the bottom and the side of the printed construct. Image acquisition was automated via a Python script, which synchronized camera triggering and data storage. To enable robust analysis, the acquired images were processed using a pipeline developed in Python. The RGB channels were first separated, followed by binarization using Otsu's adaptive thresholding algorithm (implemented through OpenCV, version 4.10.0.0.84). This preprocessing step enabled accurate segmentation of printed structures and edge detection.

Printability was evaluated using both qualitative and quantitative metrics. For qualitative assessment, expert-based visual classification was employed to evaluate pattern integrity and defect types. For quantitative analysis, a customized Python script was developed to automatically extract dimensionless indicators reflecting local and global print fidelity. A total of 10 quantitative metrics were calculated based on the methods summarized in Table 1, providing a multi-dimensional assessment of printed geometry across a variety of bioinks and support baths.

4.5 AI models

All AI models in this study were implemented using Python. RF models were constructed with the Scikit-learn library (version 1.5.1), while the MLP and LSTM-MLP hybrid models were developed using the PyTorch framework (version 2.3.1). For all models, the Adam optimizer was used with an initial learning rate of 0.0005, which was dynamically adjusted during training. Specifically, the learning rate gradually decreased as the number of epochs increased, following a learning rate decay strategy to improve convergence. The MSE loss function was used to quantify the difference between predicted and actual indicators of printability. Additionally, a strategy for stopping the learning prematurely was established, whereby training was halted if there was no improvement in validation loss for 50 consecutive epochs.

All training, validation, and testing tasks were executed on a high-performance workstation equipped with an Intel Core i9-13900K CPU and an NVIDIA GeForce RTX 3090 Ti GPU (24 GB VRAM).

The dataset used for training, validation, and testing was constructed by averaging the rheological parameters and printability indicators from three independent replicates per material condition. This approach ensured robustness and reproducibility.

The baseline model was a feedforward MLP network comprising two hidden layers with 32 and 16 nodes, respectively. Dropout regularization was applied to mitigate overfitting, and rectified linear unit (ReLU) activation functions were used in all hidden layers. A sigmoid activation function was used in the output layer to map predictions of the dimensionless printability indicators to a normalized range of [0, 1].

For the cascaded LSTM-MLP neural model, we first extracted rheological sequences of length 50 (with a feature dimension of 2: shear stress and viscosity) from the raw rheological data via interval sampling. These sequences served as input to the LSTM module, which was followed by a fully connected layer to convert the LSTM outputs into a vector representing seven rheological fitting parameters. This vector was subsequently passed into an MLP module, whose architecture mirrored the baseline model but employed a single hidden layer with 16 nodes. This modular design allowed the model to learn temporal patterns in the raw rheological data and infer their effects on downstream printability outcomes.

4.6 CT characterization of 3D-printed structures

The high-resolution characterization of printed 3D structures was performed using a submicron-resolution X-ray CT system (Xradia 610 Versa, Carl Zeiss, Germany). To enhance the contrast between the bioink and the support bath in the X-ray images, 2% (mass fraction) barium sulfate (B889319, Macklin, China) was added to the bioink formulation. For each sample, a total of 1024 projection images (1024×1024 pixels) were acquired across the *Z*-axis.

CT image post-processing followed a workflow analogous to that used for photographic analysis of 2D prints. Each CT slice was binarized using a custom Python script to differentiate printed material from the background. The resulting image stack was imported into the 3D Viewer plugin of ImageJ for volumetric reconstruction and exported in stereolithography (STL) format.

The STL files were further processed in Materialize Magics to prepare them for fidelity analysis. This included automated mesh healing, surface smoothing (smoothing parameter: 50 µm), and mesh simplification (50% reduction in polygon count), producing a clean and manageable 3D model.

To assess the fidelity of the printed construct, the reconstructed model was spatially aligned with its corresponding theoretical model using the auto-registration feature in Materialize Magics. A surface-to-surface deviation heat map was generated using the "Part Comparison" function to visualize local discrepancies in printing accuracy. In addition, two Boolean subtraction operations were performed to identify regions of material excess and unfilled voids. The volumes of these regions were computed and summed to yield the total error volume, which served as a quantitative measure of overall 3D print fidelity.

Supplementary Information The online version contains supplementary material available at https://doi.org/10.1631/bdm.2500456.

Acknowledgements This work was supported by the National Natural Science Foundation of China (Nos. 52305314 and U21A20394), the Beijing Natural Science Foundation (Nos. 7252285 and L246001), and the National Key Research and Development Program of China (No. 2023YFB4605800).

Author contributions YCF and ZX conceived and designed the overall project. XHZ developed the cascaded neural network framework and, together with SCM, implemented the computational code. XHZ, JTY, SCM, and LXM performed the experiments and collected the data. XHZ prepared the initial draft of the manuscript, with revisions and editorial input from ZXW, YCF, and ZX. BYW and ZRZ provided theoretical support and critical insights. The project was jointly supervised by TZ, YCF, and ZX. All authors contributed to data interpretation, discussed the results, and approved the final manuscript.

Declarations

Conflict of interest ZX is an editorial board member of *Bio-Design and Manufacturing* (*BDM*). TZ is an associate editor of *BDM*. YCF is a guest editor of the Special Column on AI-Powered Biofabrication of *BDM*. They were not involved in the editorial review or the decision to publish this article. The authors declare that they have no conflict of interest.

Ethical approval This study does not contain any studies with human or animal subjects performed by any of the authors.

Data availability The raw rheological curve data, printed pattern images collected by the imaging platform, datasets used for training the RF models and the cascaded neural network, as well as the training and validation results, have been uploaded to a public GitHub repository at https://github.com/William-blue/AI_embedded-bioprinting. Source data are provided with this paper.

Code availability The code used for binarizing printed pattern images and extracting quantitative evaluation indicators, as well as the codes of the RF models and the cascaded neural network, have also been uploaded to the public GitHub repository at https://github.com/William-blue/AI_embedded-bioprinting.

Use of generative AI tools During the preparation of this work, the authors used ChatGPT to check for grammatical errors and improve readability. After using this tool, the authors reviewed and edited the content as needed and take full responsibility for the content of the publication.

References

1. Budharaju H, Sundaramurthi D, Sethuraman S (2024) Embedded 3D bioprinting−an emerging strategy to fabricate biomimetic & large vascularized tissue constructs. *Bioact Mater* 32:356–384. https://doi.org/10.1016/j.bioactmat.2023.10.012
2. Zeng XB, Meng ZJ, He JK et al (2022) Embedded bioprinting for designer 3D tissue constructs with complex structural organization. *Acta Biomater* 140:1–22. https://doi.org/10.1016/j.actbio.2021.11.048
3. Duraivel S, Laurent D, Rajon DA et al (2023) A silicone-based support material eliminates interfacial instabilities in 3D silicone printing. *Science* 379(6638):1248–1252. https://doi.org/10.1126/science.ade4441
4. O'Bryan CS, Bhattacharjee T, Hart S et al (2017) Self-assembled micro-organogels for 3D printing silicone structures. *Sci Adv* 3(5):e1602800. https://doi.org/10.1126/sciadv.1602800
5. Bhattacharjee T, Zehnder SM, Rowe KG et al (2015) Writing in the granular gel medium. *Sci Adv* 1(8):e1500655. https://doi.org/10.1126/sciadv.1500655
6. Li Q, Yu SY, Wang YX et al (2025) Programmable embedded bioprinting for one-step manufacturing of arterial models with customized contractile and metabolic functions. *Trends Biotechnol* 43(4):918–945. https://doi.org/10.1016/j.tibtech.2024.11.019
7. Fang YC, Ji MK, Yang Y et al (2023) 3D printing of vascularized hepatic tissues with a high cell density and heterogeneous microenvironment. *Biofabrication* 15(4):045004. https://doi.org/10.1088/1758-5090/ace5e0
8. Schwab A, Levato R, D'Este M et al (2020) Printability and shape fidelity of bioinks in 3D bioprinting. *Chem Rev* 120(19): 11028–11055. https://doi.org/10.1021/acs.chemrev.0c00084
9. Lee SC, Gillispie G, Prim P et al (2020) Physical and chemical factors influencing the printability of hydrogel-based extrusion bioinks. *Chem Rev* 120(19):10834–10886. https://doi.org/10.1021/acs.chemrev.0c00015
10. Wu Y, Yang X, Gupta D et al (2024) Dissecting the interplay mechanism among process parameters toward the biofabrication of high-quality shapes in embedded bioprinting. *Adv Funct Mater* 34(21):2313088. https://doi.org/10.1002/adfm.202313088.
11. Gillispie G, Prim P, Copus J et al (2020) Assessment methodologies for extrusion-based bioink printability. *Biofabrication* 12(2):022003. https://doi.org/10.1088/1758-5090/ab6f0d
12. Lei IM, Zhang D, Gu WX et al (2023) Soft hydrogel shapeability via supportive bath matching in embedded 3D printing. *Adv Mater Technol* 8(15):2300001. https://doi.org/10.1002/admt.202300001
13. Naghieh S, Chen XB (2021) Printability–a key issue in extrusion-based bioprinting. *J Pharm Anal* 11(5):564–579. https://doi.org/10.1016/j.jpha.2021.02.001
14. Li XR, Zheng FY, Wang XD et al (2023) Biomaterial inks for extrusion-based 3D bioprinting: property, classification, modification, and selection. *Int J Bioprinting* 9(2):649. https://doi.org/10.18063/ijb.v9i2.649
15. Zhou K, Sun YD, Yang JQ et al (2022) Hydrogels for 3D embedded bioprinting: a focused review on bioinks and support baths. *J Mater Chem B* 10(12):1897–1907. https://doi.org/10.1039/D1TB02554F
16. Yogeshwaran S, Goodarzi Hosseinabadi H, Gendy DE et al (2024) Design considerations and biomaterials selection in embedded extrusion 3D bioprinting. *Biomater Sci* 12(18):4506–4518.

https://doi.org/10.1039/d4bm00550c
17. Ren B, Song KD, Sanikommu AR et al (2022) Study of sacrificial ink-assisted embedded printing for 3D perfusable channel creation for biomedical applications. *Appl Phys Rev* 9(1): 011408. https://doi.org/10.1063/5.0068329
18. Shin S, Hyun J (2021) Rheological properties of cellulose nanofiber hydrogel for high-fidelity 3D printing. *Carbohydr Polym* 263:117976. https://doi.org/10.1016/j.carbpol.2021.117976
19. Li Q, Ma L, Gao ZQ et al (2022) Regulable supporting baths for embedded printing of soft biomaterials with variable stiffness. *ACS Appl Mater Interfaces* 14(37):41695–41711. https://doi.org/10.1021/acsami.2c09221
20. Jin YF, Chai WX, Huang Y (2017) Printability study of hydrogel solution extrusion in nanoclay yield-stress bath during printing-then-gelation biofabrication. *Mater Sci Eng C* 80:313–325. https://doi.org/10.1016/j.msec.2017.05.144
21. Bone JM, Childs CM, Menon A et al (2020) Hierarchical machine learning for high-fidelity 3D printed biopolymers. *ACS Biomater Sci Eng* 6(12):7021–7031. https://doi.org/10.1021/acsbiomaterials.0c00755
22. Fang YC, Guo YH, Wu BY et al (2023) Expanding embedded 3D bioprinting capability for engineering complex organs with freeform vascular networks. *Adv Mater* 35(22):e2205082. https://doi.org/10.1002/adma.202205082
23. Zhang ZR, Zhou XH, Fang YC et al (2025) AI-driven 3D bioprinting for regenerative medicine: from bench to bedside. *Bioact Mater* 45:201–230. https://doi.org/10.1016/j.bioactmat.2024.11.021
24. Filippi M, Mekkattu M, Katzschmann RK (2025) Sustainable biofabrication: from bioprinting to AI-driven predictive methods. *Trends Biotechnol* 43(2):290–303. https://doi.org/10.1016/j.tibtech.2024.07.002
25. Zhou C, Liu CR, Liao ZD et al (2025) AI for biofabrication. *Biofabrication* 17(1):012004. https://doi.org/10.1088/1758-5090/ad8966
26. Bonatti AF, Vozzi G, de Maria C (2024) Enhancing quality control in bioprinting through machine learning. *Biofabrication* 16(2):022001. https://doi.org/10.1088/1758-5090/ad2189
27. Abalymov A, van der Meeren L, Skirtach AG et al (2020) Identification and analysis of key parameters for the ossification on particle functionalized composites hydrogel materials. *ACS Appl Mater Interfaces* 12(35):38862–38872. https://doi.org/10.1021/acsami.0c06641
28. Khalvandi A, Tayebi L, Kamarian S et al (2023) Data-driven supervised machine learning to predict the compressive response of porous PVA/Gelatin hydrogels and in-vitro assessments: employing design of experiments. *Int J Biol Macromol* 253: 126906. https://doi.org/10.1016/j.ijbiomac.2023.126906
29. Liu SH, Zhang HG, Ahlfeld T et al (2023) Evaluation of different crosslinking methods in altering the properties of extrusion-printed chitosan-based multi-material hydrogel composites. *Bio-Des Manuf* 6(2):150–173. https://doi.org/10.1007/s42242-022-00194-3
30. Gholami K, Ege F, Barzegar R (2023) Prediction of composite mechanical properties: integration of deep neural network methods and finite element analysis. *J Compos Sci* 7(2):54. https://doi.org/10.3390/jcs7020054
31. Seifermann M, Reiser P, Friederich P et al (2023) High-throughput synthesis and machine learning assisted design of photodegradable hydrogels. *Small Methods* 7(9):e2300553. https://doi.org/10.1002/smtd.202300553
32. Entekhabi E, Haghbin Nazarpak M, Sedighi M et al (2020) Predicting degradation rate of genipin cross-linked gelatin scaffolds with machine learning. *Mater Sci Eng C* 107:110362. https://doi.org/10.1016/j.msec.2019.110362
33. Karaoglu IC, Kebabci AO, Kizilel S (2023) Optimization of gelatin methacryloyl hydrogel properties through an artificial neural network model. *ACS Appl Mater Interfaces* 15(38): 44796–44808. https://doi.org/10.1021/acsami.3c12207
34. Martineau RL, Bayles AV, Hung CS et al (2022) Engineering gelation kinetics in living silk hydrogels by differential dynamic microscopy microrheology and machine learning. *Adv Biol* 6(1): e2101070. https://doi.org/10.1002/adbi.202101070
35. Sabbagh F, Muhamad II, Nazari Z et al (2018) From formulation of acrylamide-based hydrogels to their optimization for drug release using response surface methodology. *Mater Sci Eng C* 92:20–25. https://doi.org/10.1016/j.msec.2018.06.022
36. Soleimani S, Heydari A, Fattahi M (2023) Swelling prediction of calcium alginate/cellulose nanocrystal hydrogels using response surface methodology and artificial neural network. *Ind Crops Prod* 192:116094. https://doi.org/10.1016/j.indcrop.2022.116094
37. Boztepe C, Daskin M, Erdogan A et al (2021) Preparation of poly(acrylamide-co-2-acrylamido-2-methylpropan sulfonic acid)-g-Carboxymethyl cellulose/Titanium dioxide hydrogels and modeling of their swelling capacity and mechanic strength behaviors by response surface method technique. *Polym Eng Sci* 61(7): 2083–2096. https://doi.org/10.1002/pen.25736
38. Islamkulov M, Karakuş S, Özeroğlu C (2023) Design artificial intelligence-based optimization and swelling behavior of novel crosslinked polymeric network hydrogels based on acrylamide-2-hydroxyethyl methacrylate and acrylamide-N-isopropylacrylamide. *Colloid Polym Sci* 301(3):259–272. https://doi.org/10.1007/s00396-023-05064-7
39. Zhang JR, Liu Y, Chandra Sekhar PD et al (2023) Rapid, autonomous high-throughput characterization of hydrogel rheological properties via automated sensing and physics-guided machine learning. *Appl Mater Today* 30:101720. https://doi.org/10.1016/j.apmt.2022.101720
40. Wang JK, Zhu BG, Hui CY et al (2023) Determination of material parameters in constitutive models using adaptive neural network machine learning. *J Mech Phys Solids* 177:105324. https://doi.org/10.1016/j.jmps.2023.105324
41. Mahmoudabadbozchelou M, Jamali S (2021) Rheology-Informed Neural Networks (RhINNs) for forward and inverse metamodelling of complex fluids. *Sci Rep* 11(1):12015. https://doi.org/10.1038/s41598-021-91518-3
42. Qiao Q, Zhang X, Yan ZH et al (2023) The use of machine learning to predict the effects of cryoprotective agents on the GelMA-based bioinks used in extrusion cryobioprinting. *Bio-Des Manuf* 6(4):464–477. https://doi.org/10.1007/s42242-023-00244-4
43. Nadernezhad A, Groll J (2022) Machine learning reveals a general understanding of printability in formulations based on rheology additives. *Adv Sci* 9(29):2202638. https://doi.org/10.1002/advs.202202638
44. Kelly D, Sergis V, Ventura i Blanco L et al (2025) Autonomous control of extrusion bioprinting using convolutional neural networks. *Adv Funct Mater* 35(30):2424553. https://doi.org/10.1002/adfm.202424553
45. Sergis V, Kelly D, Pramanick A et al (2025) In-situ quality monitoring during embedded bioprinting using integrated microscopy and classical computer vision. *Biofabrication* 17(2): 025004.

https://doi.org/10.1088/1758-5090/adaa22

46. Lee J, Oh SJ, An SH et al (2020) Machine learning-based design strategy for 3D printable bioink: elastic modulus and yield stress determine printability. *Biofabrication* 12(3):035018. https://doi.org/10.1088/1758-5090/ab8707
47. Zhang YM, Wang ZX, Hu QF et al (2022) 3D bioprinted GelMA-nanoclay hydrogels induce colorectal cancer stem cells through activating Wnt/β-catenin signaling. *Small* 18(18):2200364. https://doi.org/10.1002/smll.202200364
48. Prendergast ME, Burdick JA (2022) Computational modeling and experimental characterization of extrusion printing into suspension baths. *Adv Healthc Mater* 11(7):2101679. https://doi.org/10.1002/adhm.202101679
49. Zhu JJ, Li YH, Xie WJ et al (2022) Low-swelling adhesive hydrogel with rapid hemostasis and potent anti-inflammatory capability for full-thickness oral mucosal defect repair. *ACS Appl Mater Interfaces* 14(48):53575–53592. https://doi.org/10.1021/acsami.2c18664
50. Gao Q, Niu XF, Shao L et al (2019) 3D printing of complex GelMA-based scaffolds with nanoclay. *Biofabrication* 11(3): 035006. https://doi.org/10.1088/1758-5090/ab0cf6
51. Hua WJ, Zhang C, Cui HR et al (2025) High-speed embedded ink writing of anatomic-size organ constructs. *Adv Sci* 12(13): 2405980. https://doi.org/10.1002/advs.202405980
52. Guo ZW, Dong LN, Xia JJ et al (2021) 3D printing unique nanoclay-incorporated double-network hydrogels for construction of complex tissue engineering scaffolds. *Adv Healthc Mater* 10(11):e2100036. https://doi.org/10.1002/adhm.202100036
53. Lin XY, Zhang D, Chen XY et al (2024) Self-cross-linked oxidized sodium alginate/gelatin/halloysite hydrogel as injectable, adhesive, antibacterial dressing for hemostasis. *ACS Sustain Chem Eng* 12(31):11739–11753. https://doi.org/10.1021/acssuschemeng.4c03668
54. Pardo A, Bakht SM, Gomez-Florit M et al (2022) Magnetically-assisted 3D bioprinting of anisotropic tissue-mimetic constructs. *Adv Funct Mater* 32(50):2208940. https://doi.org/10.1002/adfm.202208940
55. Cidonio G, Cooke M, Glinka M et al (2019) Printing bone in a gel: using nanocomposite bioink to print functionalised bone scaffolds. *Mater Today Bio* 4:100028. https://doi.org/10.1016/j.mtbio.2019.100028
56. Xu RZ, Dou BH, Yu S et al (2025) Enabling 3D printability and vascular morphogenesis with double network dynamic hydrogels. *Mater Today* 84:10–27. https://doi.org/10.1016/j.mattod.2025.01.019
57. Cadena MA, Sing A, Taylor K et al (2024) A 3D bioprinted cortical organoid platform for modeling human brain development. *Adv Healthc Mater* 13(27):2401603. https://doi.org/10.1002/adhm.202401603
58. Wu BY, Zeng ZX, Fang YC et al (2024) Omnidirectional elastic constraint-based embedded 3D printing in non-yield stress fluids for engineering complex tissues. *Mater Today* 80:74–86. https://doi.org/10.1016/j.mattod.2024.08.005
59. Trikalitis VD, Kroese NJJ, Kaya M et al (2023) Embedded 3D printing of dilute particle suspensions into dense complex tissue fibers using shear thinning xanthan baths. *Biofabrication* 15(1): 015014. https://doi.org/10.1088/1758-5090/aca124
60. Lai GY, Meagher L (2024) Versatile xanthan gum-based support bath material compatible with multiple crosslinking mechanisms: rheological properties, printability, and cytocompatibility study. *Biofabrication* 16(3):035005. https://doi.org/10.1088/1758-5090/ad39a8
61. Wu Q, Song KD, Zhang DM et al (2022) Embedded extrusion printing in yield-stress-fluid baths. *Matter* 5(11):3775–3806. https://doi.org/10.1016/j.matt.2022.09.003
62. Yu SL, Chai HY, Xiong YQ et al (2022) Studying complex evolution of hyperelastic materials under external field stimuli using artificial neural networks with spatiotemporal features in a small-scale dataset. *Adv Mater* 34(26):e2200908. https://doi.org/10.1002/adma.202200908
63. Yu XJ, Zhao YT, Abudouaini H et al (2024) A novel spherical GelMA-HAMA hydrogel encapsulating APET×2 polypeptide and CFIm25-targeting sgRNA for immune microenvironment modulation and nucleus pulposus regeneration in intervertebral discs. *J Nanobiotechnol* 22(1):556. https://doi.org/10.1186/s12951-024-02783-z
64. Antunes J, Gaspar VM, Ferreira L et al (2019) In-air production of 3D co-culture tumor spheroid hydrogels for expedited drug screening. *Acta Biomater* 94:392–409. https://doi.org/10.1016/j.actbio.2019.06.012
65. Lee A, Hudson AR, Shiwarski DJ et al (2019) 3D bioprinting of collagen to rebuild components of the human heart. *Science* 365(6452):482–487. https://doi.org/10.1126/science.aav9051